Lithium-Ion Battery Cell Open Circuit Fault Diagnostics: Methods, Analysis, and Comparison

Shiyao Zhou, Ziqiang Chen, *Senior Member, IEEE*, and Tiantian Lin

***Abstract*—Battery fault diagnosis has great significance for guaranteeing the safety and reliability of lithium-ion battery (LIB) systems. Out of many possible failure modes of the series–parallel connected LIB pack, cell open circuit (COC) fault is a significant part of the causes that lead to the strong inconsistency in the pack and the reduction of pack life. Therefore, it is extremely important to diagnose COC faults in real time. Motivated by this fact, we propose Kirchhoff's law based method, short-time Fourier transform based method, the Pearson correlation coefficient based method, dual extended Kalman filter (DEKF) based method, and long short-term memory recurrent neural network based method for diagnosing COC fault. These diagnostic approaches do not rely on other sensor data except pack current and terminal voltages of modules composed of cells in parallel. Furthermore, several experiments on a 4S-3P battery pack are taken under time-varying ambient temperature conditions to evaluate and compare the computation cost, diagnostic delay, and accuracy of these approaches. Test results show that only the DEKF-based approach owns the weakest robustness, and Kirchhoff's law based method with the merit of the lowest diagnostic delay and computation cost is the most appropriate approach for online COC fault diagnosis.**

***Index Terms*—Battery fault diagnosis, diagnostic delay, lithium-ion battery, open circuit fault.**

I. Introduction

THE Li-ion battery (LIB) has been widely used in electric automobiles, unmanned aerial vehicles, robots, and engineering machinery due to its high power density, high energy density, long cycle life, and no memory effect [1], [2]. As a complex electrochemical system, LIB has certain risks of instability properties resulting in cell irreversible degradation, even more, leading to internal short circuit and thermal runaway, when the battery system is operated outside of the safe operating area [3], including thermal abuse, electrical abuse, and mechanical abuse [4]. Hence, the passive and active safety designs of LIB storage systems are attracting more and more attention [5].

To meet the voltage level and energy level demands of energy storage devices, some manufacturers use LIBs connected in series to compose the battery pack, whereas some other manufacturers, considering the passive safety protection, compose the LIB pack by connecting small capacity cells in a series–parallel connection with fusible link wires [6]. The fusible link wire constitutes the current loop between the bus bar and cell electrodes as shown in Fig. 1(a) [7]. When series cell failure occurs, such as internal/external short circuits, thermal runaways, and severe mechanical shocks, the link wire will open the circuit. Then, the fault cell can be isolated from the battery pack, as shown in

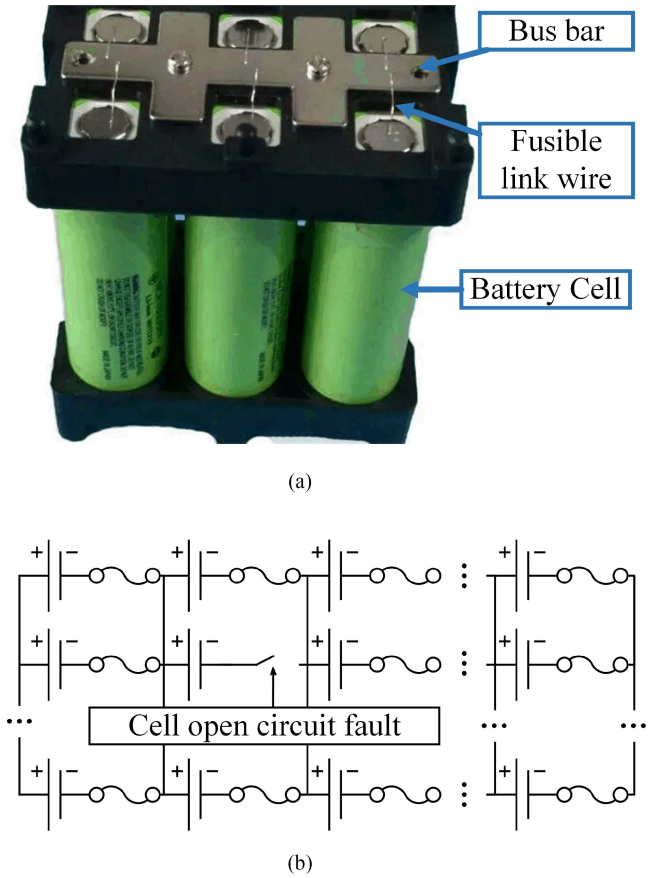

Fig. 1. (a) Passive safety design by using fusible link wires. (b) Schematic diagram for the COC fault.

Manuscript received 19 May 2022; revised 5 August 2022; accepted 27 September 2022. Date of publication 10 October 2022; date of current version 18 November 2022. This paper was presented in part at the 2021 IEEE Industrial Electronics and Applications Conference (IEACon) [DOI: 10.1109/IEACon51066.2021.9654490]. This work was supported by the National Natural Science Foundation of China under Grant 51677119. Recommended for publication by Associate Editor U. Deshpande. *(Corresponding author: Ziqiang Chen.)*

Shiyao Zhou is with the State Key Laboratory of Ocean Engineering, Shanghai Jiao Tong University, Shanghai 200240, China (e-mail: shiyaozhou_sjtu@outlook.com).

Ziqiang Chen is with the State Key Laboratory of Ocean Engineering and Collaborative Innovation Center for Advanced Ship and Deep-Sea Exploration, Shanghai Jiao Tong University, Shanghai 200240, China (e-mail: chenziqiang@sjtu.edu.cn).

Tiantian Lin is with the State Key Laboratory of Ocean Engineering, Shanghai Jiao Tong University, Shanghai 200240, China (e-mail: ttlinet@sjtu.edu.cn).

Color versions of one or more figures in this article are available at https://doi.org/10.1109/TPEL.2022.3211568.

Digital Object Identifier 10.1109/TPEL.2022.3211568

Fig. 1(b), to prevent the single cell fault from causing a failure chain reaction of other cells in the pack. Therefore, the open circuit of the fault cell will lead to capacity inconsistency and resistance inconsistency in a parallel connected pack, and we define this type of fault as the cell open circuit (COC) fault. For battery packs with large capacity, the open circuit of a single cell has an inconspicuous effect on pack electrical properties. However, with the development of LIB technology, the capacity of a single cell is gradually increasing. For instance, the package of the cylindrical cell used in Tesla is changing from 18650 to 4680 [8], and the cell capacity is rising from about 3.1 A·h to more than 20 A·h. As a result, the inconsistency caused by the COC fault will be greatly enlarged, and the harmful impacts caused by inconsistency will be significantly expanded. On the other hand, for those tiny-scale LIB storage systems, where only several cells are connected in parallel, the adverse influence caused by the COC fault cannot be ignored. Thus, it is essential to diagnose the COC fault accurately and instantaneously with low computational costs.

Most battery system faults can be diagnosed by abnormal performances of the sensor data [9]. Normally, fault diagnostics for battery systems can be separated into three categories: signal processing based method, model-based method, and data-driven based method [10].

Signal processing based methods utilize the fault information contained in sensor data to conduct the fault analysis [11]. Special treatments, such as time–frequency domain transform, analyzing statistical feature, perform on the measurement data to extract abnormal information [12]. The statistical analysis methods typically include standard deviation [13], Pearson correlation coefficient (PCC) [14], interclass correlation coefficient [15], sample entropy [16], and Shannon entropy [17]. Thus, LIB faults can be diagnosed by changes in statistical information. Time–frequency domain transform methods are normally employed to obtain the amplitude–frequency characteristic and phase–frequency characteristic of sensor data [18]. The abnormality of these characteristics illustrates the potential for fault. Although the Fourier transform [19] and the Wavelet transform [20] are widely used for battery sensor data processing, these algorithms are rarely applied for battery fault diagnosis. On the other hand, many existing studies use time–frequency domain transform to process the sensor signals for calculating LIB impedance [21], which can be utilized to determine the fault of the battery system as well.

The main principles of model-based methods are utilizing filters or observers to estimate states or parameters of physical base models, and generating residuals between physical base models output and measured data [22]. Then, battery system abnormalities can be determined by analyzing the residuals or estimated states and parameters. The utilizing of filters or observers, such as extended Kalman filter (EKF) [23], particle filter [24], Lunberger observer [25], etc., can reduce the residual based methods sensitivity to observation noise and process noise. Dey et al. designed a sliding mode observer-based diagnostor to detect and isolate the faults of a temperature sensor, voltage sensor, and current sensor [9], and designed a partial differential equation model based observer to diagnose thermal faults in Li-ion batteries [26]. Feng et al. [27] built a coupled electrochemical–thermal model to study the internal short circuits with different degrees, and the parameters of the equivalent circuit model (ECM) estimated by RLS were applied for internal short circuits fault diagnosis. Yang et al [28] utilized a fractional-order model to diagnose cell external short circuit fault, and a random forest model was applied to recognize the electrolyte leakage behavior.

With the gradual and in-depth development of machine learning in recent years, data-driven algorithms have become deeply entrenched in our lives nowadays [29], such as data mining, image recognition, and natural language processing. Data-driven methods do not require explicit models to describe battery behaviors [30], and these methods can directly diagnose battery faults or estimate battery states by using sampling data. Therefore, data-driven methods can help these nonspecialists in battery management quickly develop a specific function for LIB systems. However, the implementation of this method generally requires a proper preprocessing of raw data for LIBs to extract useful features [31], and requires a proper machine learning model to acquire a better regression on historical data. The preprocessing of raw data includes normalization, labeling, clustering, filtering outliers, information fusion, and dimensionality reduction. The widely used machine learning models for LIB fault diagnosis include artificial neural network [32], support vector machine (SVM) [33], and Gaussian process regression (GPR) [34]. Machine learning models can be selected according to the characteristics of the data set. For instance, SVM and GPR are suitable for small data sets with a small amount of classification [35]. Due to the neglect of fault mechanisms, some data-driven methods require a large amount of training set [31], accompanied by a high computational cost for training and data manually preprocessing.

However, few researchers have paid attention to COC fault diagnosis. In our previous study [7], the COC fault is proposed for the first time, and a PCC-based method is applied to diagnose the COC fault. Whether the PCC-based method is the optimal diagnostic method for COC fault remains to be further studied. To solve this problem, we analyze the COC fault characteristics, and several diagnosis approaches are proposed and specifically improved according to these characteristics. Three types of signal processing based methods, a model-based method, and a data-driven based method are proposed to diagnose COC fault in the series–parallel connected LIB pack. Proposed signal processing based methods contain Kirchhoff's law based method, fast time Fourier transform based method, and PCC-based method. The Thevenin ECM and dual extended Kalman filter (DEKF) are applied as a model-based method. The recurrent neural network with long short-term memory (RNN-LSTM) cells is utilized as the data-driven based method. Furthermore, considering that temperature sensors are sparsely placed in-pack in practice, the proposed methods do not rely on other sensor data except pack current and terminal voltages to enhance the environmental suitability. Four test cases under complex operation conditions with a 4S-3P LIB pack are implemented to verify the accuracy, diagnostic delay, and computation cost of the proposed approaches.

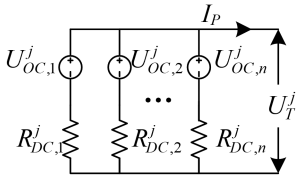

Fig. 2. Equivalent circuit of the LIB module.

The remainder of this article is organized as follows: Section II illustrates the diagnostic methods for COC faults. Section III details the scheme of the test bench and illustrates the analytical results of the proposed methods. Section IV concludes this article.

II. Preliminary Analysis and Diagnostic Methods

A. COC Fault Characteristic Analysis

Here, "module" is defined as a small pack composed of cells connected in parallel. When a COC fault occurs, the capacity of the fault module is reduced and the module impedance is increased instantaneously. Thereafter, the capacity inconsistency and impedance inconsistency between the fault module and healthy modules will significantly deteriorate. The inconsistency caused by COC faults is instantaneous and it is different from the slowly varying inconsistency caused by cell electrochemical degradation. Therefore, the COC fault is possibly detected from the perspective of instantaneous inconsistency. Compared with impedance, battery capacity is hard to observe accurately and rapidly. Thus, module impedance and module terminal voltage may be more suitable for COC fault diagnosis.

B. Signal Processing Based Method

1) Kirchhoff's Law Based Approach: Based on the aforementioned analysis, it is feasible to perform a COC fault diagnosis based on dc resistance inconsistency between modules. Several methods can be applied for obtaining LIB resistance, such as recursive least-squares methods, state observers, and variant Kalman filters. However, these methods require a high computational cost. To improve the real-time performance of the COC fault detector in practice, Kirchhoff's law based method is utilized to calculate module resistances. First, we model the module by using the Rint model as shown in Fig. 2.

Then, we can describe the equivalent circuit by Kirchhoff's law as follows:

$$\begin{cases} I_{P,k-1} = \frac{U^j_{T,k-1}-U^j_{\mathrm{OC},1,k}}{R^j_{DC,1,k}} + \frac{U^j_{T,k-1}-U^j_{\mathrm{OC},2,k}}{R^j_{DC,2,k}} + \cdots \frac{U^j_{T,k-1}-U^j_{\mathrm{OC},n,k}}{R^j_{DC,n,k}} \\ I_{P,k} = \frac{U^j_{T,k}-U^j_{\mathrm{OC},1,k}}{R^j_{\mathrm{DC},1,k}} + \frac{U^j_{T,k}-U^j_{\mathrm{OC},2,k}}{R^j_{\mathrm{DC},2,k}} + \cdots \frac{U^j_{T,k}-U^j_{\mathrm{OC},n,k}}{R^j_{\mathrm{DC},n,k}} \end{cases} \tag{1}$$

where k indicates the timescale for the calculation time t_k, $R^j_{\mathrm{DC},i}$ represents the dc resistance of cell i in the jth module, $U^j_{\mathrm{OC},i}$ represents the open circuit voltage of cell i in the jth module, $R^j_{\mathrm{DC},i}$ and $U^j_{\mathrm{OC},i}$ are supposed as constants from t_{k-1} to t_k, U^j_T represents the terminal voltage of the jth module, and I_P represents the battery pack current (discharge is positive, charge is negative). We suppose $I_{P,k} \neq I_{P,k+1}$. Then, (1) can be rewritten as

$$\left(\frac{1}{R^j_{\mathrm{DC},1,k}} + \frac{1}{R^j_{\mathrm{DC},2,k}} + \cdots \frac{1}{R^j_{\mathrm{DC},n,k}}\right)^{-1} = R^j_{\mathrm{DC},k} = \frac{U^j_{T,k} - U^j_{T,k-1}}{I_{P,k} - I_{P,k-1}}. \tag{2}$$

The left-hand side items in (2) are the resistance of the jth module at t_k ($R^j_{\mathrm{DC},k}$). However, if the resistance is updated when the current mutation is small, the calculated resistance can be easily disturbed by the LIB polarization phenomenon. As a result, a current threshold should be set to monitor the pack current mutation, and a first-order inertial filter is employed to reduce the resistance update sensitivity to noise, as formulated in the following equation:

$$R^j_{\mathrm{DC},k} = \begin{cases} w\frac{U^j_{T,k}-U^j_{T,k-1}}{I_{P,k}-I_{P,k-1}} + (1-w)\ R^j_{\mathrm{DC},k-1}, & |I_{P,k} - I_{P,k-1}| \geq I_{THR} \\ R^j_{\mathrm{DC},k-1}, & |I_{P,k} - I_{P,k-1}| < I_{\mathrm{THR}} \end{cases} \tag{3}$$

where I_{THR} denotes the current threshold for resistance update, and w is the weight of the inertial filter. The threshold value of 0.2 C is recommended on account of the computational accuracy of resistance and calculation cost as well. Then, the details for Kirchhoff's law based COC fault diagnostic process are proposed as follows:

Step 1: Calculate module resistances using (3).

Step 2: Calculate the inconsistency of resistance ΔR^j_{DC} between the jth and the (j+1)th modules:

$$\Delta R^j_{\mathrm{DC}} = R^j_{\mathrm{DC}} - R^{j+1}_{\mathrm{DC}}$$

Step 3: Calculate the standard deviation ΔR^j_{DC} within the time window from t_{k-L+1} to t_k:

$$\sigma^j_{\Delta R,k} = \sqrt{\frac{1}{L-1}\sum_{i=k-L+1}^{k}\left(\Delta R^j_{\mathrm{DC},i} - \overline{\Delta R}^j_{\mathrm{DC},i}\right)^2}$$

where $\overline{\Delta R}^j_{\mathrm{DC}}$ represents the mean value of the variable ΔR^j_{DC} within the time window from t_{k-L+1} to t_k. The recursive formula of standard deviation is obtained as

$$\sigma^j_{\Delta R,k} = \sqrt{\frac{(L-1)\kappa^j_k - L^2\left(\overline{\Delta R}^j_{\mathrm{DC},k}\right)^2}{(L-1)^2}}$$

$$\begin{cases} \overline{\Delta R}^j_{\mathrm{DC},k} = \overline{\Delta R}^j_{\mathrm{DC},k-1} + \Delta R^j_{\mathrm{DC},k}/L - \Delta R^j_{\mathrm{DC},k-L}/L \\ \kappa^j_k = \kappa^j_{k-1} + \left(\Delta R^j_{\mathrm{DC},k}\right)^2 - \left(\Delta R^j_{\mathrm{DC},k-L}\right)^2. \end{cases}$$

Step 4: ΔR^j_{DC} is evaluated through a fault detector to diagnose COC fault:

$$\overline{\Delta R}^j_{\mathrm{DC},k} - 5\sigma^j_{\Delta R,k} \underset{H_1}{\overset{H_0}{\lessgtr}} \Delta R^j_{\mathrm{DC},k} \underset{H_2}{\overset{H_0}{\lessgtr}} \overline{\Delta R}^j_{\mathrm{DC},k} + 5\sigma^j_{\Delta R,k} \tag{4}$$

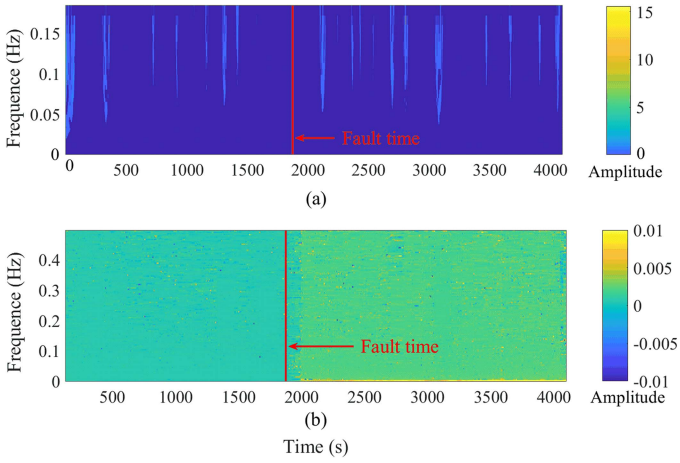

Fig. 3. Comparison between continuous wavelet transform (CWT) and STFT.

where H_1 and H_2 indicates abnormal, and H_0 indicates normal. If $\Delta R^{j}_{\mathrm{DC},k}$ triggers H_1 and $\Delta R^{j+1}_{\mathrm{DC},k}$ triggers H_2 as well, it means that the COC fault is detected in the jth module.

Step 5: Return to Step 1, $k = k{+}1$.

Here, the last module in-pack is supposed as a neighbor of the first module. If simply preset a threshold for module resistance inconsistency rather than using the standard deviation, the inconsistency caused by module degradation differences can easily trigger the threshold. Furthermore, considering the confidence level of 3σ principle is only 99.7%, which may easily generate misdiagnoses, a $\pm 6\sigma$ confidence interval is used in Step 4.

2) Short-Time Fourier Transform (STFT) Based Approach: Considering that Kirchhoff's law based approach is motivated by pack current mutation, this method may lose efficacy if the pack current changes slowly. As a result, we attempt to explore whether the impedance calculated by the time–frequency domain analysis can perform COC fault diagnosis as well. The impedance inconsistency between LIB modules can be extracted by the time–frequency transform. In this study, an STFT-based approach is applied for calculating the impedance inconsistency.

Fourier transform and wavelet transform are widely applied for converting sensor signals from the time domain to the frequency domain. Wavelet transform can carry out a multiscale detailed analysis of the unsteady signal to achieve the purpose of refining small fault information in the fault signal [11]. For sound, vibration, and image signals, wavelet transform is more suitable for extracting the time–frequency characteristics. However, for impedance calculation, the wavelet transform can only extract impedance amplitude information, whereas the Fourier transform can separate the capacitive impedance, inductive impedance, and resistive impedance. As shown in Fig. 3, the resistive impedance is more applicable for COC fault than the amplitude of impedance. Fig. 3(a) shows the impedance calculated by CWT. Obviously, the transform results have no relevance to the COC fault. Fig. 3(b) shows the resistive impedance calculated by STFT. Apparently, the time–frequency spectrum is mutated after the COC fault has happened. As a result, the STFT is utilized to diagnose COC faults. Considering signals under high-frequency domains contains too much measurement noise as shown in Fig. 3(b), high-frequency signals need to be screened out. Furthermore, the scales of impedance increase under low frequency are larger, which indicates higher diagnostic robustness. Therefore, we use the resistive impedance under the five lowest frequencies (0 Hz is not included) to diagnose the COC fault.

The calculation period of STFT is chosen as $(1{-}C_{\mathrm{win}})L$, where C_{win} is the time window coverage and L is the length of the time window. Hanning window is selected as the time window function, window length L is set to 256, and C_{win} is set to 15/16. The details for STFT-based diagnostic strategy are proposed as follows.

Step 1: Transform module terminal voltage sequence $(U^{j}_{T,k-L+1}, U^{j}_{T,k-L+2}, \ldots, U^{j}_{T,k})$ and pack current sequence $(I_{P,k-L+1}, I_{P,k-L+2}, \ldots, I_{P,k})$ within the time window into sinusoidal signals by using fast Fourier transform, and generate vector $\mathbf{A}^{j}_{U}$, $\mathbf{A}_{I}$, $\boldsymbol{\varphi}^{j}_{U}$, $\boldsymbol{\varphi}_{I}$ ($\mathbf{A}$ is amplitude vector, φ is phase position vector).

Step 2: Calculate the modulus resistive impedances $Z^{j,f}_{AC,k}, f = 1/(Lf_s), 2/(Lf_s), \ldots, 5/(Lf_s))$:

$$Z^{j,f}_{AC,k} = \mathrm{A}^{j,f}_{U} \cos(\varphi^{j,f}_{U} - \varphi_{I})/\mathrm{A}_{I} \tag{5}$$

where f indicates the signal frequency, and f_s is the sampling frequency of the terminal voltage and the pack current.

Step 3: Calculate the resistive impedance inconsistency $\Delta Z^{j,f}_{\mathrm{AC},k}$ between the jth and the $(j{+}1)$th modules.

Step 4: $\Delta Z^{j,f}_{\mathrm{AC},k}$ is evaluated through a fault detector as (6) to diagnose COC fault.

$$\overline{\Delta Z}^{j,f}_{\mathrm{AC},k} - Z^{f}_{\mathrm{THR}} \underset{H^{f}_{1}}{\overset{H_0}{\lessgtr}} \Delta Z^{j,f}_{\mathrm{AC},k} \underset{H^{f}_{2}}{\overset{H_0}{\lessgtr}} \overline{\Delta Z}^{j,f}_{\mathrm{AC},k} + Z^{f}_{\mathrm{THR}}$$

$$\overline{\Delta Z}^{j,f}_{\mathrm{AC},k} = \sum_{f=k-L+1}^{k} \Delta Z^{j,f}_{\mathrm{AC},k} \tag{6}$$

where Z^{f}_{THR} is the threshold value under different frequencies. If all $\Delta Z^{j}_{\mathrm{AC},k}$ have triggered H^{f}_{1} and all $\Delta Z^{j+1}_{\mathrm{AC},k}$ have triggered H^{f}_{2}, a COC fault can be identified in the jth module. In this study, the threshold value is set to ± 0.5 mΩ.

Step 5: Return to Step 1, $k = k{+}(1{-}C_{\mathrm{win}})L$.

3) Pearson Correlation Coefficient (PCC) Based Approach: The variations of module capacity and impedance caused by COC fault would lead to voltage fluctuations with different amplitudes and the state of charge (SoC) offset between the healthy module and a faulty module. Although SoC bias can make an impact on open circuit voltage, which causes the mean value inconsistency between module terminal voltages, the slowly varying characteristic of the SoC bias will lead to the long diagnostic latency. Accordingly, the terminal voltage fluctuations of neighboring modules can be compared by using PCC for the sake of extracting statistical information differences

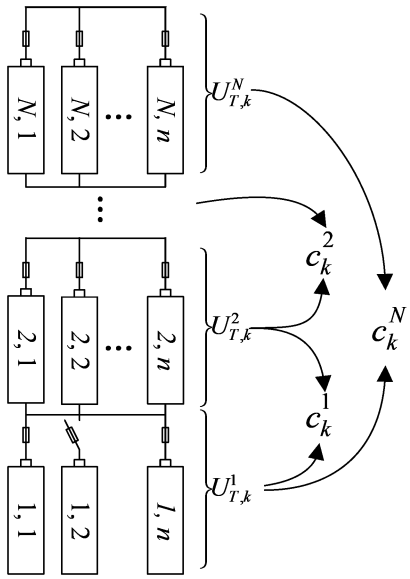

Fig. 4. Rules for PCC generation.

between neighboring modules. PCC is a statistical method indicating the linear relation between two variable sequences [36]. A larger PCC indicates a lower possibility of a fault has happened. Then, we can diagnose a COC fault according to the PCC value. The voltage correlation coefficients between adjacent modules can be calculated as shown in Fig. 4. The expression of PCC is

$$c_k^j=\frac{\sum_{i=k-L+1}^{k}\left(U_{T,i}^j-\overline{U}_{T,k}^j\right)\left(U_{T,i}^{j+1}-\overline{U}_{T,k}^{j+1}\right)}{\sqrt{\sum_{i=k-L+1}^{k}\left(U_{T,i}^j-\overline{U}_{T,k}^j\right)^2}\sqrt{\sum_{i=k-L+1}^{k}\left(U_{T,i}^{j+1}-\overline{U}_{T,k}^{j+1}\right)^2}} \tag{7}$$

where $\overline{U}_{T,k}^j$ represents the mean value of U_T^j within the time window from $t_{k\text{-}L+1}$ to t_k. The recursive formula of c_k^j is formulated as

$$\begin{cases}\kappa_{1,k}^j=\kappa_{1,k-1}^j+U_{T,k}^{*j}U_{T,k}^{*j+1}-U_{T,k-L}^{*j}U_{T,k-L}^{*j+1}\\ \kappa_{2,k}^j=\kappa_{2,k-1}^j+U_{T,k}^{*j}-U_{T,k-L}^{*j}\\ \kappa_{3,k}^j=\kappa_{3,k-1}^j+\left(U_{T,k}^{*j}\right)^2-\left(U_{T,k-L}^{*j}\right)^2\\ \kappa_{4,k}^j=\kappa_{4,k-1}^j+U_{T,k}^{*j+1}-U_{T,k-L}^{*j+1}\\ \kappa_{5,k}^j=\kappa_{5,k-1}^j+\left(U_{T,k}^{*j+1}\right)^2-\left(U_{T,k-L}^{*j+1}\right)^2\\ c_k^j=\frac{L\kappa_{1,k}^j-\kappa_{2,k}^j\kappa_{4,k}^j}{\sqrt{L\kappa_{3,k}^j-\left(\kappa_{2,k}^j\right)^2}\sqrt{L\kappa_{5,k}^j-\left(\kappa_{4,k}^j\right)^2}}\end{cases} \tag{8}$$

$$U_{T,k}^{*j}=\begin{cases}U_{T,k}^j & |I_{P,k}-I_{P,k-1}|<I_{\text{THR}}\\ U_{T,k}^j+A_{sq}\cos(\pi k), & |I_{P,k}-I_{P,k-1}|<I_{\text{THR}}\end{cases} \tag{9}$$

where A_{sq} is a constant and $A_{sq}=5R^j$. We suppose that $r^j\sim \mathrm{N}(0,R^{j,2})$ is the observation noise of U_T^j ($U_{T,k}^j=\widehat{U}_{T,k}^j+r_k^j$), and r^j is independent of U_T^j. $\widehat{U}_T^j$ is the true value of the terminal voltage. A periodic square wave with the amplitude $\pm A_{sq}$ should be superimposed on U_T^j as shown in (9) if the LIB pack is maintained in an idle state for a long time. Otherwise, the PCC will close to zero, and may easily increase the potential of misdiagnosis [37]. The pack idle state is determined by the current threshold expressed in (9). The current threshold I_{THR} is set to 0.1 C. In this way, we can eliminate the decline of PCC caused by measurement noise and enhance the robustness of the diagnostic approach.

The last procedure for COC fault detection is to locate the fault module. Suppose that c_k^j and c_k^{j+1} triggers the pre-set threshold, whereas the other PCCs are still within the normal range. It means that a COC fault might have occurred in the *j*th module. The threshold is set to 0.978, and the length of the time window is set to 120 empirically.

C. Data-Driven Based Method

In recent years, the studies of data-driven algorithms in battery systems have gradually increased, and most of them are focused on state estimation and remaining useful life prediction. Among normally used neural network models, LSTM-RNN is the most suitable for modeling long-time sequence behavior precisely and solving multiclassification problems. LSTM-RNN is first proposed to solve the problem of gradient disappearance by Hochreiter et al. in 1997 [38].

In this study, we utilize LSTM-RNN to identify the module terminal voltage inconsistency caused by the COC fault. The model design of LSTM-RNN is proposed in Fig. 5(a). The mapping type of the LSTM-RNN used in this study is the "many to many" type. The pack current and voltage bias between modules are used as model inputs. It should be noted that module terminal voltage cannot be directly used as LSTM-RNN inputs. Considering that the highly nonlinear electrochemical characteristics of the battery cell can cover up COC fault features, the voltage bias is adopted to counteract the battery's nonlinear electrochemical characteristics. Otherwise, the diagnostic accuracy of LSTM-RNN will be extremely low or the nonconvergence of loss function often occurs in the training process. The LSTM-RNN calculates the probabilities of three types of labels, which are classed into "Abnormal #1", "Abnormal #2," and "Normal." The label with the highest probability will be output as the diagnostic results. The reason for using two abnormal classes is that the features of $U_T^j-U_T^{j+1}$ and $U_T^{j-1}-U_T^j$ are diametrically opposite when the *j*th module is the fault module. All LSTM-RNN inputs need to be standardized first. Discrete standardization is applied to linear transform the pack current into the range of [0–1]. The maximum value used in discrete standardization is the rated maximum discharge current of the battery pack, and the minimum value is the rated maximum charge current. Mean–variance standardization is employed to transform the voltage bias. The mean value is set to zero, and the variance is set to the noise covariance between different voltage acquisition channels. The outputs of the LSTM-RNN network are transferred to a fully connected linear layer, and the output size is set to 10. The number of nerves in the linear layer is set to 96. The linear layer is followed by a softmax layer to calculate

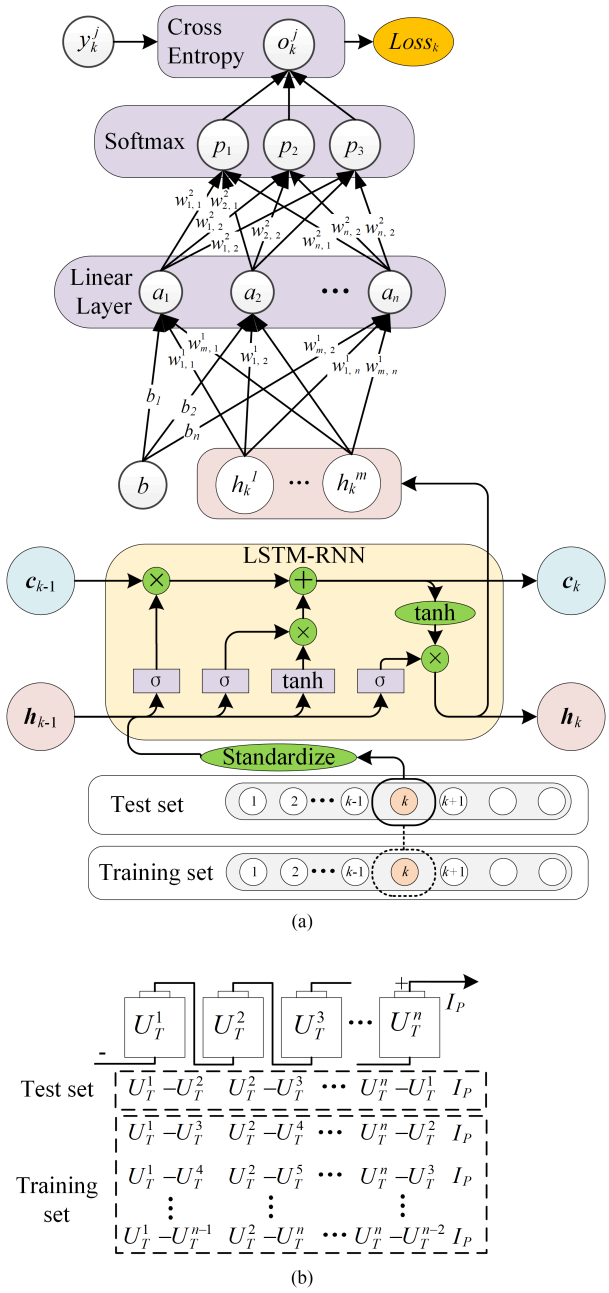

Fig. 5. (a) Network schematic of LSTM-RNN based fault detector; (b) Division of the training and test dataset.

the probabilities of three labels separately. The number of neural cells in the softmax layer is three. The output of the network is the class with a higher probability.

The test sets of the LSTM-RNN are terminal voltage bias between neighboring modules and the pack current under multiple test cases. The training sets are terminal voltage inconsistency between nonadjacent modules and the pack current as shown in Fig. 5(b). In the training process, the cross entropy is selected as the loss function and y_k^j is the pre-set label of the training set. Adam is selected as the network optimizer. The initial learning rate is set to 0.005. The maximum training epoch is set to 1000. The batch size is the amount of training set groups. Fig. 6 shows

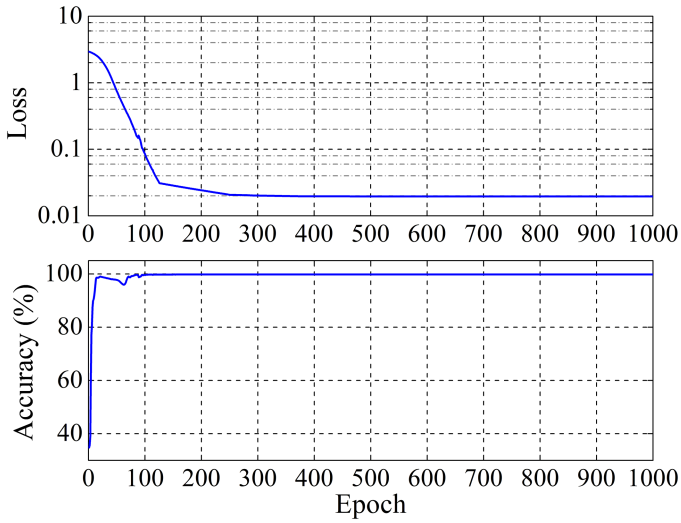

Fig. 6. Training process of the LSTM-RNN.

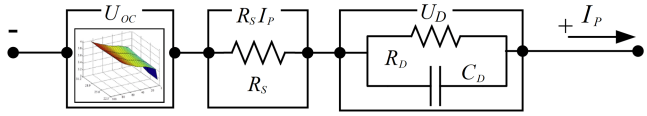

Fig. 7. ECM for battery module.

the training process of the proposed LSTM-RNN, and the final training accuracy is close to 100%. If outputs o_k^j and o_k^{j-1} are "Abnormal #1" and "Abnormal #2" separately, it means that a COC fault may have happened in the *j*th module. Otherwise, in other cases, we affirm that no COC fault has occurred in the *j*th module, even though o_k^j and o_k^{j-1} are both "Abnormal #1" or "Abnormal #2."

D. Model-Based Method

In this article, the voltage residuals between the ECM and measured terminal voltages are devoted to COC fault diagnosis. DEKF is utilized to generate voltage residuals. When the values or statistical information of residues generated by DEKF are anomalous, it means that a fault may have happened. One-state Thevenin ECM, with the merit of high accuracy and low computational cost, has been widely employed in model-based methods. In this study, the LIB module is treated as a big cell modeled by one-state Thevenin ECM as shown in Fig. 7 , where R_S is the ohmic resistance, R_D is the polarization resistance, and C_D is the polarization capacitance. $U_{\rm OC}$ is the open circuit voltage, related to SoC. It can be formulated as

$$U_{OC}(z,T) = \kappa_0 + \kappa_1 z + \kappa_2 z^2 + \kappa_3 z^3 + \kappa_4 z^4 + \kappa_5/z + \kappa_6 \mathrm{In}(z) + \kappa_7 \mathrm{In}(1-z)$$

where z represents SoC, T indicates module surface temperature, and κ_i can be acquired by OCV test. The relation between module SoC and pack current I_P is formulated as follows:

$$z(t) = z(t_0) - \int_{t_0}^{t} \frac{\eta(I_C)}{C_N} I_C(\tau) d\tau$$

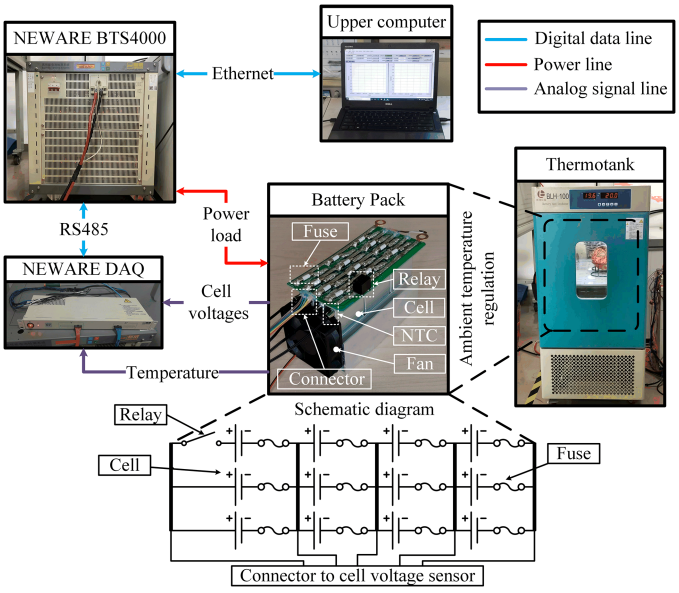

Fig. 8. Framework of the test bench.

where C_N is the battery cell nominal capacity. The state-space model is formulated to describe the dynamics of the states vector x and parameters vector θ:

$$x_k = \begin{bmatrix} \left(1 - e^{-\frac{\Delta t}{R_{D,k-1}C_{D,k-1}}}\right) & 0 \\ 0 & 1 \end{bmatrix} x_{k-1} + \begin{bmatrix} R_{D,k-1}\left(1 - e^{-\frac{\Delta t}{R_{D,k-1}C_{D,k-1}}}\right) \\ -\Delta t\eta/C_N \end{bmatrix} I_{P,k-1} + \omega_{k-1}$$

$$\theta_k = \theta_{k-1} + \upsilon_k$$

$$U_{T,k} = U_{OC}(z_k, T_k) + U_{D,k} + R_{s,k}I_{P,k} + r_k$$

where $x = [U_D, \mathrm{SoC}]^{\mathrm{T}}$ and $\theta = [R_S, R_D, C_D]^{\mathrm{T}}$. The steps of DEKF using the above-mentioned state-space model are summarized in Table I [23], [39].

Then, a preset threshold is compared with the residual voltage calculated in Step 4. If the value of the voltage residual larger than the threshold, it means that a COC fault may have happened. Here, the voltage residual threshold is set to ± 15 mV. To enhance the DEKF-based method robustness, the sum of squared residual (SSR) of the voltage residual sequence will be calculated to reconfirm the COC fault, after the threshold for the residual voltage is triggered. Considering that the statistical distribution of residuals is related to battery loads, the variance of residuals is not suitable for fault reconfirms. SSR can be calculated by

$$s(k) = \frac{1}{L}\sum_{j=k-L+1}^{k} e_j e_j^T.$$

SSR is evaluated through (10) to diagnose COC fault

$$s(k) \underset{H_1}{\overset{H_0}{\lessgtr}} \mu \tag{10}$$

where H_1 indicates abnormal, H_0 indicates normal, μ is the threshold for SSR, and μ is set to 50 according to experiments.

TABLE I
DUAL EXTENDED KALMAN FILTER (DEKF)

Nonlinear state-space model

$$\begin{cases} x_k = f(x_{k-1}, \theta_{k-1}, I_{P,k-1}) + \omega_{k-1} \\ \theta_k = \theta_{k-1} + \nu_{k-1} \\ y_k = g(x_k, \theta_{k-1}, I_{P,k}) + r_k \end{cases}$$

Based on nonlinear state-space model, we define:

$$H_k = \left.\frac{dg(x, \hat{\theta}_k^-, I_{B,k})}{dx}\right|_{\hat{x}_k^-}, \quad A_k = \left.\frac{df(x, \hat{\theta}_k^-, I_{B,k})}{dx}\right|_{\hat{x}_k^-},$$

$$B_k = \left.\frac{df(\hat{x}_{k-1}^+, \theta, I_P)}{dI_P}\right|_{I_{P,k}},$$

$$C_k = \left.\frac{\partial g(\hat{x}_k^+, \theta, I_{P,k})}{\partial \theta}\right|_{\hat{\theta}_k^-} + \left.\frac{\partial g(x_k, \theta, I_{P,k})}{\partial x_k}\frac{dx_k}{d\theta}\right|_{\hat{\theta}_k^-}$$

Step 1 Initialization

For n=0, set $\hat{\theta}_0^+ = \mathrm{E}[\theta_0]$, $J_0^+ = \mathrm{E}[(\theta_0 - \hat{\theta}_0^+)(\theta_0 - \hat{\theta}_0^+)^{\mathrm{T}}]$, $\hat{x}_0^+ = \mathrm{E}[x_0]$, $P_0^+ = \mathrm{E}[(x_0 - \hat{x}_0^+)(x_0 - \hat{x}_0^+)^{\mathrm{T}}]$

Step 2 Prior estimation time update. For k = 1, 2 ,……, compute

State estimation: $\hat{x}_k^- = f(\hat{x}_{k-1}^+, \hat{\theta}_{k-1}^+, I_{P,k-1})$

State error covariance: $P_k^- = A_k P_{k-1}^+ A_k^{\mathrm{T}} + Q_{k-1}$

Parameter estimation: $\hat{\theta}_k^- = \hat{\theta}_{k-1}^+$

Parameter error covariance: $J_k^- = J_{k-1}^+ + V$

Step 3 State posteriori estimation time update

Error innovation: $e_k^- = y_k - g(\hat{x}_k^-, \hat{\theta}_k^-, I_{P,k})$

State Kalman gain matrix: $K_k = P_k^-(H_k)^{\mathrm{T}}[H_k P_k^-(H_k)^{\mathrm{T}} + R_{k-1}]^{-1}$

State estimation: $\hat{x}_k^+ = \hat{x}_k^- + K_k e_k^-$

State Error covariance: $P_k^+ = (I - K_k H_k) P_k^-$

Step 4 Parameter posteriori estimation time update

Error innovation: $e_k^+ = y_k - g(\hat{x}_k^+, \hat{\theta}_k^-, I_{P,k})$

Parameter Kalman gain matrix: $L_k = J_k^-(C_k)^{\mathrm{T}}[C_k J_k^-(C_k)^{\mathrm{T}} + W]^{-1}$

Parameter estimation: $\hat{\theta}_k^+ = \hat{\theta}_k^- + L_k e_k^+$

Parameter error covariance: $J_k^+ = (I - L_k C_k) J_k^-$

Step 5 Time update: k=k+1, return to step 2.

If H_1 is detected by (10) shortly after the threshold is triggered, the COC fault can be confirmed.

Although analyzing the abnormalities of estimated states or parameters can locate the fault as well, the variations of states and parameters will be disturbed by historical data during the early fault period, which is illustrated in our previous study [7].

III. Battery Pack Test and Diagnostic Verification

A. Setup of the Test Bench

To verify the performance of different COC fault detection strategies, a test bench is designed to simulate the fault characteristic of cell COC fault as shown in Fig. 8. The number of cells in the parallel module is three, and our modules are connected in series to compose the battery pack. Details of the test cell are given in Table II. A ceramic fuse is placed between the cell anode tab and busbar. A relay is placed between a cell's cathode tab and bus bar in the 1st module. The opening of the relay can separate a cell from the 1st module to generate the COC fault.

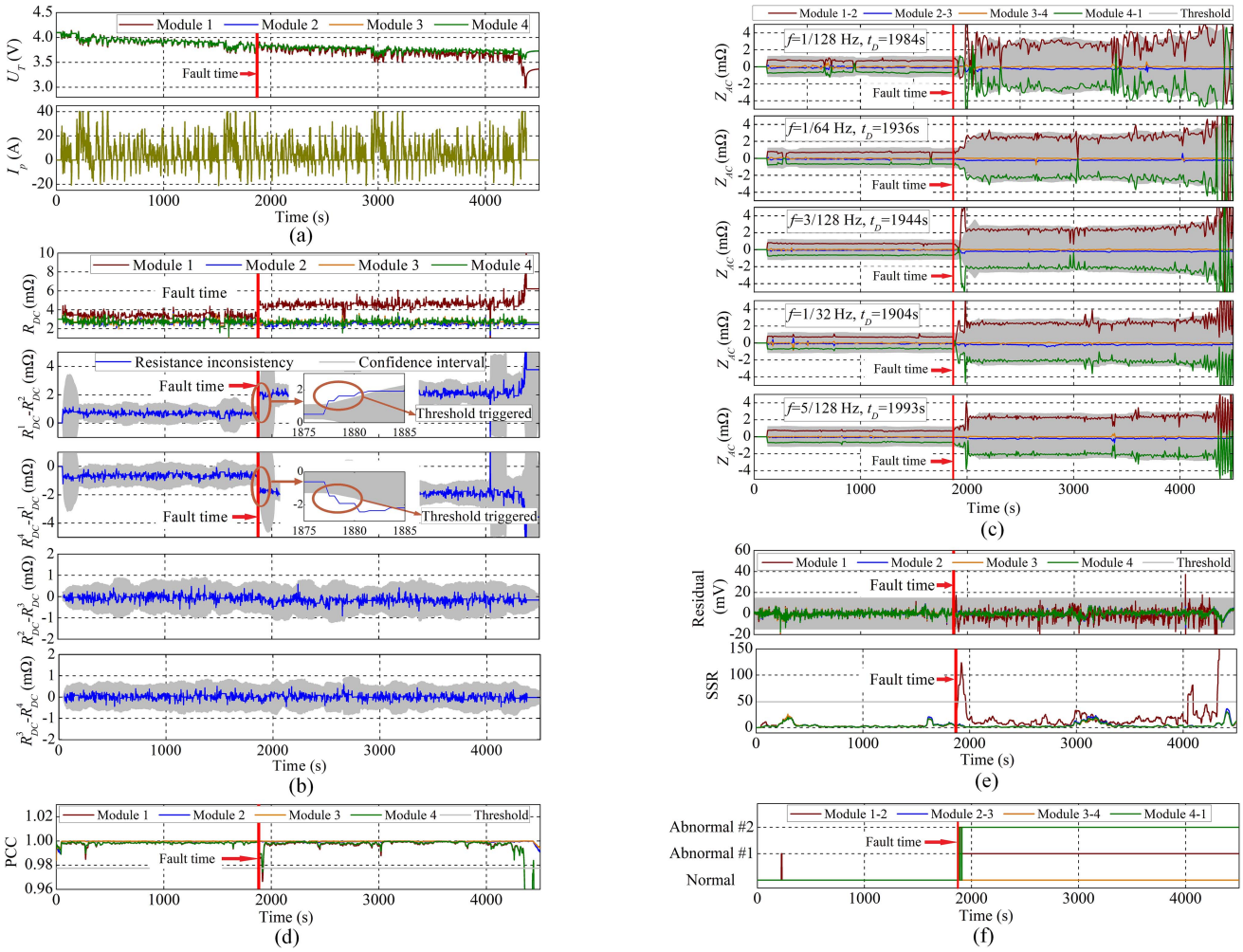

Fig. 9. COC fault diagnosis results in Case 1. (a) Measured pack current and module voltages. (b) Diagnosis results of Kirchhoff's law based method. (c) Diagnosis results of STFT based method. (d) Diagnosis results of PCC based method. (e) Diagnosis results of DEKF based method. (f) Diagnosis results of LSTM-RNN based method.

TABLE II
DETAILS OF THE TEST CELL

Parameters	Value
Battery type	Polymer LIB
Package	Soft package
Nominal capacity	3 A·h
Weight	60 g
Energy density	195 w·h/kg
Peak current range (10 s)	−30 A−15A (−10 C−5 C)
Rated current range	−15 A−6 A (−5 C−2 C)
Operating voltage range	2.75 V − 4.20 V

TABLE III
TEST CASE PROFILES

Case no.	Test cycle	Ambient temperature	Fault start time	Initial SoC
1	FUDS	25°C	1873s	87.5%
2	FUDS	9 to 25°C	498s	80.5%
3	DST	25°C	3619s	87.5%
4	DST	9 to 25°C	1311s	80.5%

The relay is maintained close until the fault command is sent out. Negative temperature coefficient resistances are temperature sensors used to measure cell surface temperature. NEWARE BTS4000 is used to load test cycles on the battery pack. Battery pack currents are measured by BTS4000. The temperatures and terminal voltages of each module are measured by NEWARE DAQ. The measurement inaccuracies of the test bench are less than 0.05%. A thermotank, which can be regulated ranging from 5°C to 65°C, is serviced for ambient temperature regulation. The fan is applied for forced-convection heat transfer of the battery pack. The sampling period of the test bench is set to 500 ms.

Four group test cases were taken as shown in Table III. Before the experiment, each module SoC is well balanced. The time of COC fault occurring is randomly set. Experiments are performed with the Federal Urban Driving Schedule (FUDS) test and Dynamic Stress Test (DST). Current profiles of FUDS and DST are provided in Figs. 9(a) and 11(a). Considering the complex operation condition in practice, Case 2 and Case 4 were taken in a time-varying temperature condition. The ambient temperature is varying from 9°C to 25°C, LIB packs with thermal management are normally operated under 5°C–35°C. The curves of ambient

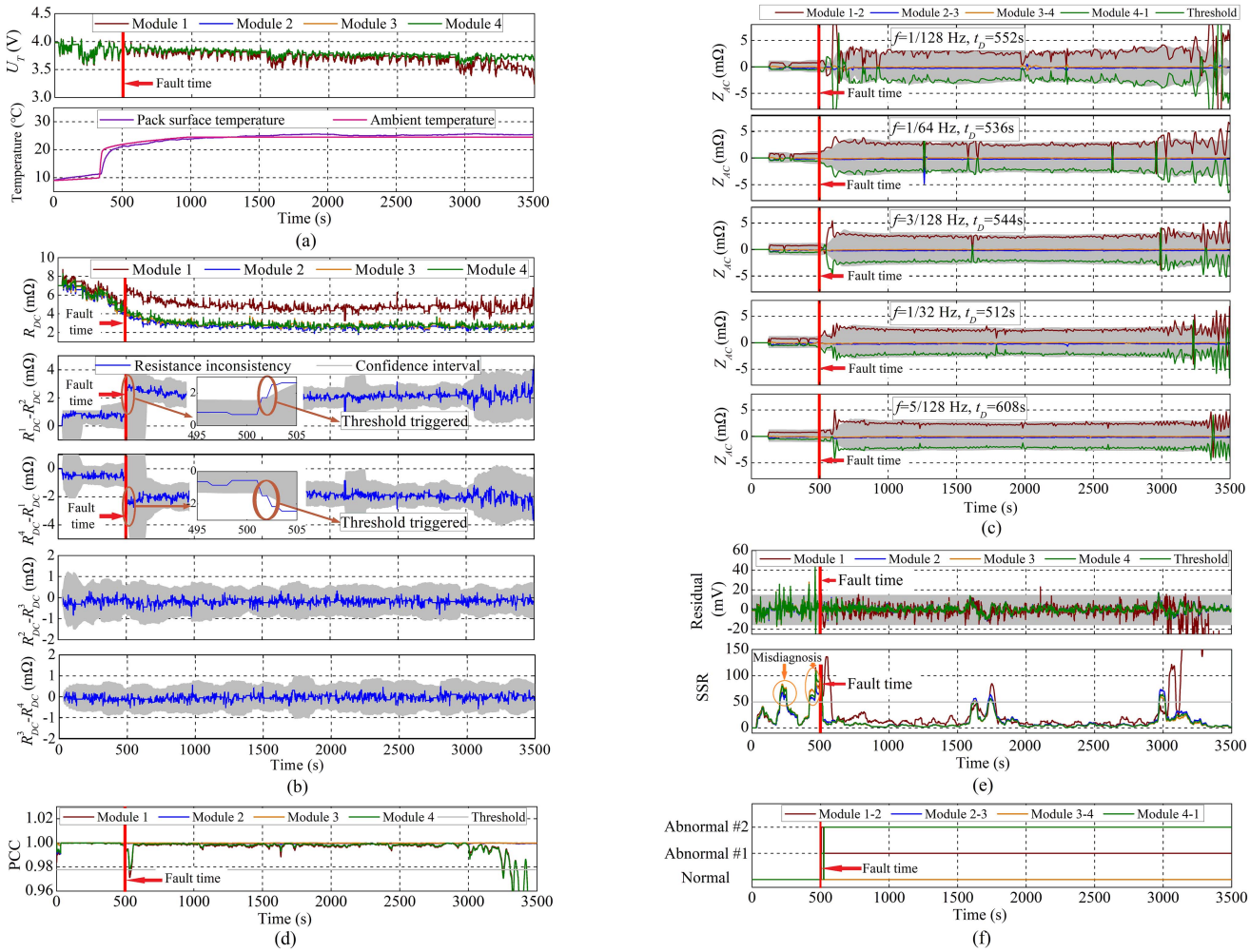

Fig. 10. COC fault diagnosis results in Case 2. (a) Measured module voltages and pack temperature. (b) Diagnosis results of Kirchhoff's law based method. (c) Diagnosis results of STFT based method. (d) Diagnosis results of PCC based method. (e) Diagnosis results of DEKF based method. (f) Diagnosis results of LSTM-RNN based method.

TABLE IV
DIAGNOSTIC DELAY OF DIFFERENT APPROACHES

Method	Case 1	Case 2	Case 3	Case 4
Kirchhoff's law	4 s	5 s	8 s	20 s
STFT	120 s	120 s	77 s	25 s
PCC	35 s	10 s	9 s	8 s
DEKF	27 s	×	×	33 s
LSTM-RNN	6 s	7 s	41 s	21 s

temperatures and the average module surface temperatures are shown in Figs. 10(a) and 12(a) separately. Case 1 and Case 3 were taken at room temperature (25°C).

B. Diagnostic Results

The diagnostic results of all cases are shown in Figs. 9–12, and the diagnostic delay of different methods under four test cases are summarized in Table IV. Diagnostic delay is defined as the time span between the start time of the fault and the time of the fault detected.

Fig. 9(a) depicts the FUDS current profile and terminal voltage profiles of the four modules in Case 1. The COC fault is occurred in 1874 s. Fig. 9(b)–(f) validates the performance of different diagnostic methods. Fig. 9(b) indicates the resistance of each module and the resistance inconsistency between modules. The time of COC fault detected by Kirchhoff's law based method is 1877s. Fig. 9(c) shows the diagnostic result of the STFT-based strategy. The fault detection time is determined by the impedance that latest triggers the threshold. Therefore, the COC fault is detected in 1993 s. Fig. 9(d) indicates the diagnostic results of PCC-based methods, and the COC fault is detected at 1898s. Fig. 9(e) shows the diagnostic result of DEKF based strategy. The residual voltages threshold is triggered in 1880 s, and the COC fault is confirmed in 1890 s by SSR. The diagnostic result of LSTM-RNN is provided in Fig. 9(f). The fault is detected in 1879 s. At the beginning of the COC fault has happened, the output of the LSTM-RNN will switch between different classes repeatedly, which is caused by the change of current flow direction. It should be mentioned that, before the fault has happened, an error signal is reported by LSTM-RNN between the 1st and 2nd modules, Meanwhile, between the 1st

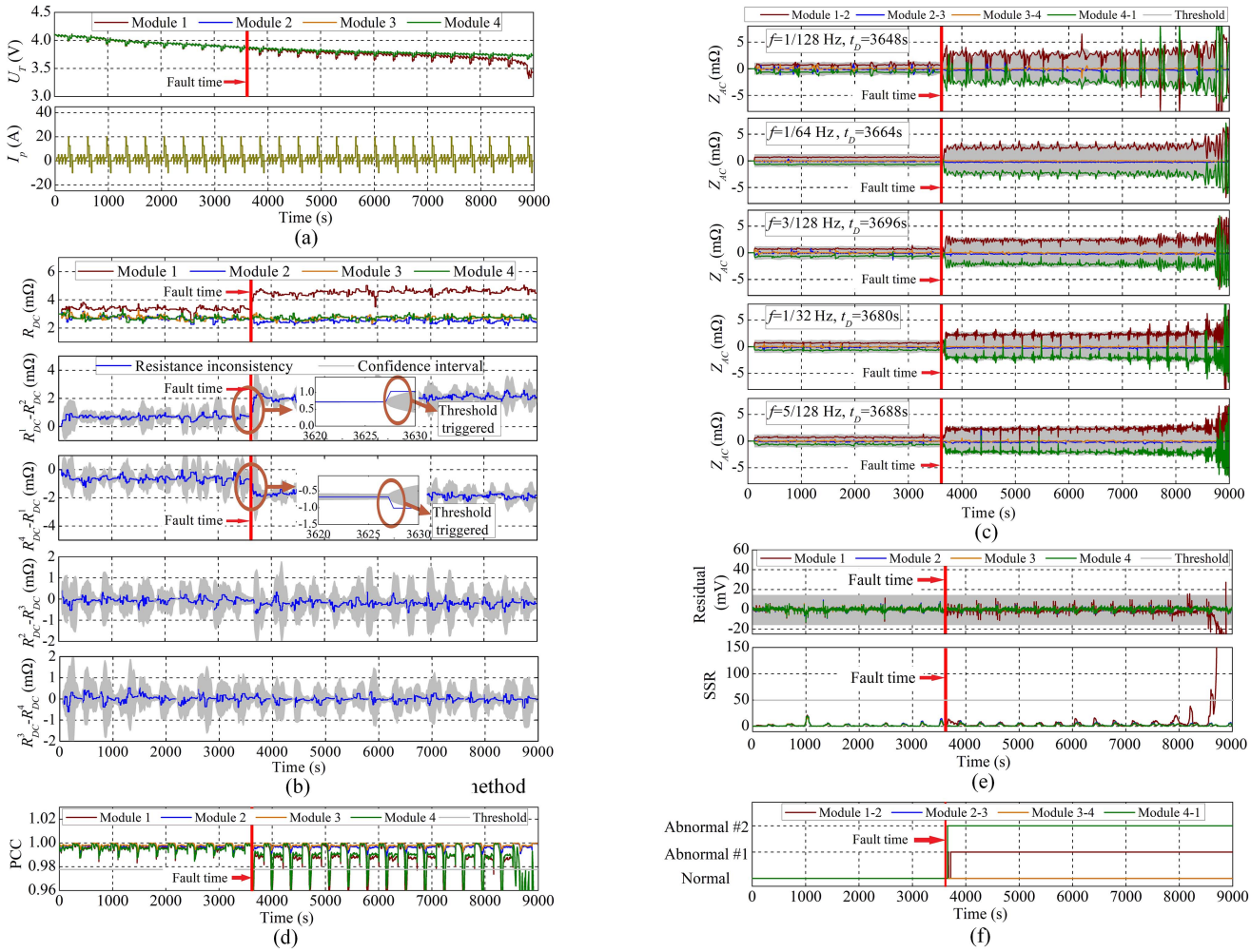

Fig. 11. COC fault diagnosis results in Case 3. (a) Measured pack current and module voltages. (b) Diagnosis results of Kirchhoff's law based method. (c) Diagnosis results of STFT based method. (d) Diagnosis results of PCC based method. (e) Diagnosis results of DEKF based method. (f) Diagnosis results of LSTM-RNN based method.

and 4th modules, a normal signal is output by LSTM-RNN. On the base of the fault detection strategy introduced in Section II-C, it is reconfirmed that no COC fault has happened, which can effectively improve the robustness of the LSTM-RNN method.

The diagnostic delay of each approach is summarized in Table IV. The Kirchhoff's law based method owns the shortest diagnostic delay in Case 1, whereas the STFT-based strategy owns the longest diagnostic delay. That's because the STFT-based strategy uses FFT for the decomposition of historical sequences. Only the proportion of fault data in historical sequences is high enough, and the COC fault can be successfully detected.

Fig. 10(a) depicts the terminal voltage profiles and temperature profiles in Case 2. The COC fault is generated at 498 s. Among the diagnostics introduced in Section II, several misdiagnoses are produced by DEKF based method as shown in Fig. 10(e). The COC fault is detected by Kirchhoff's law based method at 501 s as shown in Fig. 10(b). The COC fault is detected by the STFT-based approach at 608 s as shown in Fig. 10(c). The diagnostic results of the PCC-based strategy are provided in Fig. 10(d), and the COC fault is detected at 528 s. The diagnostic result of LSTM-RNN is provided in Fig. 10(f) and the fault is detected at 505 s. Kirchhoff's law based method owns the shortest diagnostic delay in Case 2, whereas the STFT-based strategy owns the longest diagnostic delay. The fast time-varying temperature has few negative effects on these strategies except DEKF based strategy. The voltage residual of DEKF is significantly increased under low ambition temperature.

Fig. 11(a) depicts the DST current profile and terminal voltage profiles in Case 3. The COC fault is occurred in 3619 s. Fig. 11(b) indicates that the COC fault is detected by Kirchhoff's law based method at 3627s. Fig. 11(c) indicates that the fault is detected by STFT based method at 3696s. In Fig. 11(c), the COC fault is detected at 3628s by the PCC-based method. The fault is detected at 3660s by LSTM-RNN as shown in Fig. 11(f). The DEKF-based method is unable to diagnose the COC fault under DST cycles. Kirchhoff's law based method still owns the shortest diagnostic delay in Case 3, and the STFT-based method owns the longest diagnostic delay. The misdiagnosis of DEKF means that the current load profiles have a remarkable influence on the voltage residuals generated by DEKF. A small SSR threshold

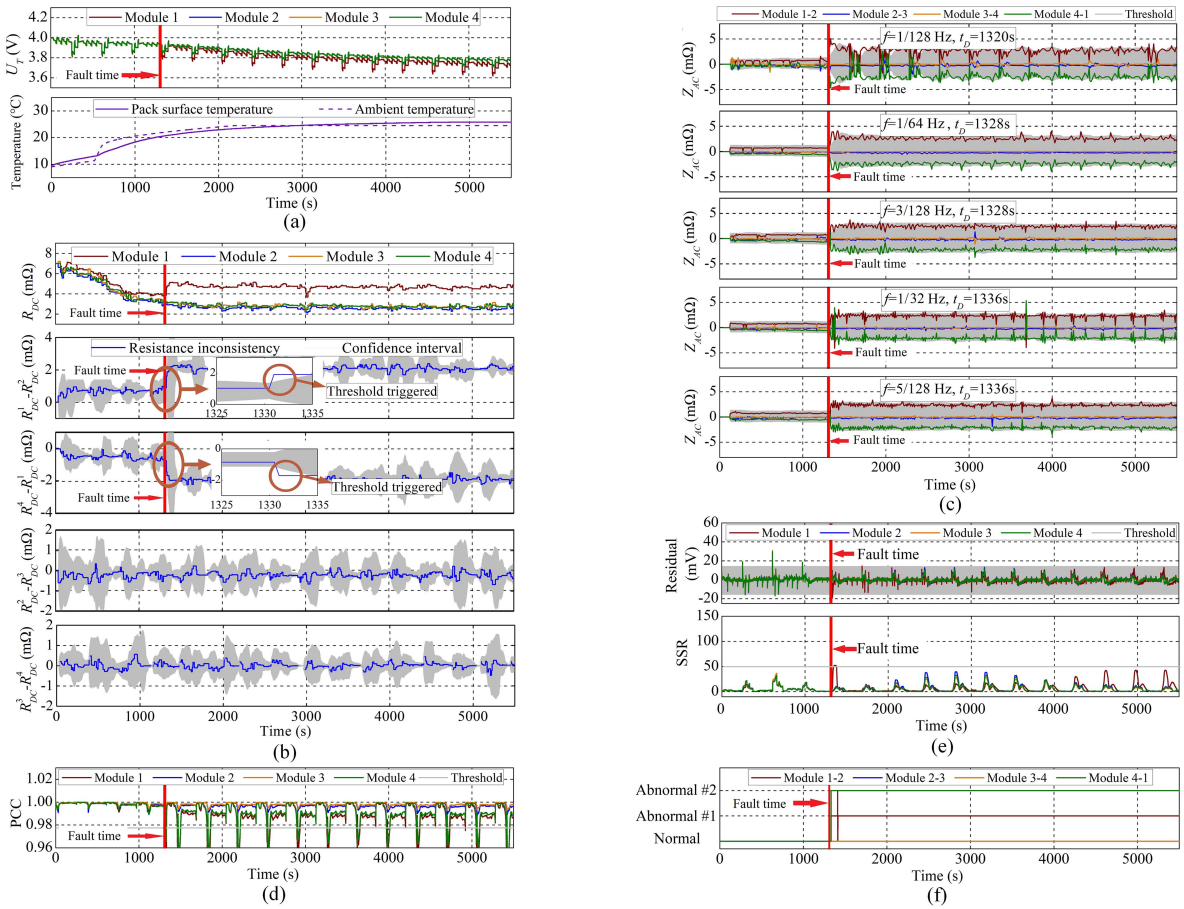

Fig. 12. COC fault diagnosis results in Case 4. (a) Measured module voltages and pack temperature. (b) Diagnosis results of Kirchhoff's law based method. (c) Diagnosis results of STFT based method. (d) Diagnosis results of PCC based method. (e) Diagnosis results of DEKF based method. (f) Diagnosis results of LSTM-RNN based method.

for DEKF based method will lead to misdiagnosis, while a large threshold will lead to missed diagnosis under certain load profiles. As a result, the DEKF-based method possesses the worst robustness among all these methods. Furthermore, the diagnostic delay of LSTM-RNN is significantly prolonged under DST cycles, which means current load profiles have an impact on LSTM-RNN diagnostic delay. The most probable reason for LSTM-RNN performance degradation is that the voltage inconsistency between battery modules is not significant under low current loads.

Fig. 12(a) shows the terminal voltage profiles and temperature profiles in Case 4. The COC fault is generated at 1311 s. The COC fault is detected by Kirchhoff's law based method at 1331 s as shown in Fig. 12(b). The COC fault is detected by the STFT-based method at 1336 s as shown in Fig. 12(c). In Fig. 12(d), the fault is detected at 1319 s by using PCC based method. In Fig. 12(e), the fault is detected by the DEFK-based method at 1344 s. The diagnostic result of LSTM-RNN is provided in Fig. 12(f) and the fault is detected at 1332s. The PCC-based method owns the shortest diagnostic delay in Case 4, whereas the DEKF-based method owns the longest diagnostic delay.

To compare the computational cost of different diagnostic methods, the offline computational time of these algorithms calculated by MATLAB is listed in Table V. The CPU of the target PC is Ryzen5-4600H, and all these algorithms are calculated by a single CPU core, whose frequency is 3.0 GHz.

TABLE V
COMPUTATION TIME OF DIFFERENT DIAGNOSTIC METHODS

Method	Case 1	Case 2	Case 3	Case 4
Kirchhoff's law	0.231 s	0.138 s	0.500 s	0.256 s
STFT	0.591 s	0.406 s	1.271 s	0.805 s
PCC	0.234 s	0.147 s	0.521 s	0.266 s
DEKF	0.351 s	0.299 s	0.691 s	0.502 s
LSTM-RNN	0.365 s	0.266 s	0.734 s	0.420 s

As provided in Table V, the computational cost of STFT based approach is the highest, whereas Kirchhoff's law based approach is the lowest. The computational cost of PCC based approach is almost the same as Kirchhoff's law based approach, and the DEKF based is almost the same as the LSTM-RNN based approach.

Through the comprehensive comparison of four test cases, the performance of the DEKF-based strategy is the worst among the algorithms introduced in Section II. There is no missed diagnosis or misdiagnosis generated by other algorithms. As shown in Table IV, the average diagnostic delay of Kirchhoff's law based method is about 9 s. It is about 15 s when using the PCC-based method. In terms of computational cost, Kirchhoff's

law based method is almost the same as the PCC. Therefore, Kirchhoff's law based method is the optimal algorithm for COC fault detection under dynamic working conditions among the algorithms proposed in this study. The average diagnostic delay of LSTM-RNN is about 19 s slightly long than PCC. However, the computational cost of the LSTM-RNN is much higher than that of the correlation coefficient based strategy. Additionally, the accuracy of the LSTM-RNN may unavoidably decrease with the degradation of the battery cell, unless the training sets contain massive battery data sets gathered under a different state of health (SoH). The average diagnostic delay of the STFT-based strategy is about 86 s. Considering STFT requires high computational cost and a long diagnostic delay, and the STFT-based strategy is unsuitable for real-time applications, especially for high voltage battery systems.

IV. Conclusion

In this article, a comparison between different types of fault diagnostic approaches for COC fault of the series–parallel connected battery pack is carried out. In general, the conclusions can be drawn as follows.

1) Kirchhoff's law based method, STFT based method, PCC-based method, DEKF-based method, and LSTM-RNN based method are proposed and improved to diagnose COC fault.
2) A 4S-3P connected LIB test bench is built up. Four groups of test cases under different operating conditions were taken to verify the performance of the five proposed approaches, including the diagnostic delay, diagnostic accuracy, and computational cost.
3) The test results indicate that Kirchhoff's law based method with the merit of the shortest diagnostic delay, lowest misdiagnostic rate, and lowest computational cost are more applicable for online COC fault detection under dynamic working conditions. The performance of PCC based method is slightly inferior to Kirchhoff's law based method. DEKF-based diagnostic method owns the worst robustness for COC fault, and the STFT owns the longest diagnosis delay and highest computational cost.

Our future work will concern with the impact of SoC and SoH inconsistency on diagnostic accuracy for COC fault.

References

[1] V. Etacheri, R. Marom, R. Elazari, G. Salitra, and D. Aurbach, "Challenges in the development of advanced Li-ion batteries: A review," *Energy Environ. Sci.,* vol. 4, no. 9, pp. 3243–3262, Sep. 2011.

[2] Z. H. Li, A. Khajepour, and J. C. Song, "A comprehensive review of the key technologies for pure electric vehicles," *Energy,* vol. 182, pp. 824–839, Sep. 2019.

[3] D. D. Lyu, B. Ren, and S. F. Li, "Failure modes and mechanisms for rechargeable lithium-based batteries: A state-of-the-art review," *Acta Mechanica,* vol. 230, no. 3, pp. 701–727, Mar. 2019.

[4] J. Zhang, L. Zhang, F. Sun, and Z. Wang, "An overview on thermal safety issues of lithium-ion batteries for electric vehicle application," *IEEE Access,* vol. 6, pp. 23848–23863, 2018.

[5] Y. S. Qiu and F. M. Jiang, "A review on passive and active strategies of enhancing the safety of lithium-ion batteries," *Int. J. Heat Mass Transfer,* vol. 184, Mar. 2022, Art. no. 122288.

[6] K. Hoshino, "Module battery with multiple cells connected in series with fuse and method of manufacturing module battery," U.S. Patent 9 793 533, Oct. 17, 2017.

[7] S. Zhou, Z. Chen, D. Huang, and T. Lin, "A fault-tolerant SoC estimation method for series-parallel connected Li-ion battery pack," *IEEE Trans. Power Electron.,* vol. 36, no. 12, pp. 13434–13448, Dec. 2021.

[8] T. G. Tranter, R. Timms, P. R. Shearing, and D. J. L. Brett, "Communication—Prediction of thermal issues for larger format 4680 cylindrical cells and their mitigation with enhanced current collection," *J. Electrochem. Soc.,* vol. 167, no. 16, Dec. 2020, Art. no. 160544.

[9] S. Dey, S. Mohon, P. Pisu, and B. Ayalew, "Sensor fault detection, isolation, and estimation in lithium-ion batteries," *IEEE Trans. Control Syst. Technol.,* vol. 24, no. 6, pp. 2141–2149, Nov. 2016.

[10] X. S. Hu, F. Feng, K. L. Liu, L. Zhang, J. L. Xie, and B. Liu, "State estimation for advanced battery management: Key challenges and future trends," *Renewable Sustain. Energy Rev.,* vol. 114, Oct. 2019, Art. no. 109334.

[11] R. Xiong, W. Z. Sun, Q. Q. Yu, and F. C. Sun, "Research progress, challenges and prospects of fault diagnosis on battery system of electric vehicles," *Appl. Energy,* vol. 279, Dec. 2020, Art. no. 115855.

[12] Z. Liu, X. Yin, Z. Zhang, D. Chen, and W. Chen, "Online rotor mixed fault diagnosis way based on spectrum analysis of instantaneous power in squirrel cage induction motors," *IEEE Trans. Energy Convers.,* vol. 19, no. 3, pp. 485–490, Sep. 2004.

[13] Z. P. Wang, J. C. Hong, L. Zhang, and P. Liu, "Voltage fault detection and precaution of batteries based on entropy and standard deviation for electric vehicles," in *Proc. 8th Int. Conf. Appl. Energy*, 2017*,* vol. 105, pp. 2163–2168.

[14] T. T. Lin, Z. Q. Chen, and S. Y. Zhou, "Voltage-correlation based multi-fault diagnosis of lithium-ion battery packs considering inconsistency," *J. Cleaner Prod.,* vol. 336, Feb. 2022, Art. no. 130358.

[15] X. Y. Li and Z. P. Wang, "A novel fault diagnosis method for lithium-ion battery packs of electric vehicles," *Measurement,* vol. 116, pp. 402–411, Feb. 2018.

[16] Y. H. Sun, H. L. Jou, and J. C. Wu, "Auxiliary diagnosis method for lead-acid battery health based on sample entropy," *Energy Convers. Manage.,* vol. 50, no. 9, pp. 2250–2256, Sep. 2009.

[17] X. Y. Li, K. W. Dai, Z. P. Wang, and W. J. Han, "Lithium-ion batteries fault diagnostic for electric vehicles using sample entropy analysis method," *J. Energy Storage,* vol. 27, Feb. 2020, Art. no. 101121.

[18] K. Mc Carthy, H. Gullapalli, and T. Kennedy, "Online state of health estimation of Li-ion polymer batteries using real time impedance measurements," *Appl. Energy,* vol. 307, Feb. 2022, Art. no. 118210.

[19] A. Rahmoun, M. Loske, and A. Rosin, "Determination of the impedance of lithium-ion batteries using methods of digital signal processing," in *Proc. 8th Int. Renewable Energy Storage Conf. Exhib.*, 2014*,* vol. 46, pp. 204–213.

[20] X. Y. Wang, X. Z. Wei, Q. J. Chen, J. G. Zhu, and H. F. Dai, "Lithium-ion battery temperature on-line estimation based on fast impedance calculation," *J. Energy Storage,* vol. 26, Dec. 2019, Art. no. 100952.

[21] X. Y. Wang et al., "A review of modeling, acquisition, and application of lithium-ion battery impedance for onboard battery management," *Etransportation,* vol. 7, Feb. 2021, Art. no. 100093.

[22] R. Isermann, "Model-based fault-detection and diagnosis - Status and applications," *Annu. Rev. Control,* vol. 29, no. 1, pp. 71–85, 2005.

[23] T. Lin, Z. Chen, C. Zheng, D. Huang, and S. Zhou, "Fault diagnosis of lithium-ion battery pack based on hybrid system and dual extended Kalman filter algorithm," *IEEE Trans. Transp. Electrific.,* vol. 7, no. 1, pp. 26–36, Mar. 2021.

[24] C. W. Zheng, Z. Q. Chen, and D. Y. Huang, "Fault diagnosis of voltage sensor and current sensor for lithium-ion battery pack using hybrid system modeling and unscented particle filter," *Energy,* vol. 191, Jan. 2020, Art. no. 116504.

[25] W. Chen, W. T. Chen, M. Saif, M. F. Li, and H. Wu, "Simultaneous fault isolation and estimation of lithium-ion batteries via synthesized design of luenberger and learning observers," *IEEE Trans. Control Syst. Technol.,* vol. 22, no. 1, pp. 290–298, Jan. 2014.

[26] S. Dey, H. E. Perez, and S. J. Moura, "Model-based battery thermal fault diagnostics: Algorithms, analysis, and experiments," *IEEE Trans. Control Syst. Technol.,* vol. 27, no. 2, pp. 576–587, Mar. 2019.

[27] X. N. Feng, C. H. Weng, M. G. Ouyang, and J. Sun, "Online internal short circuit detection for a large format lithium ion battery," *Appl. Energy,* vol. 161, pp. 168–180, Jan. 2016.

[28] R. X. Yang, R. Xiong, H. W. He, and Z. Y. Chen, "A fractional-order model-based battery external short circuit fault diagnosis approach for all-climate electric vehicles application," *J. Cleaner Prod.,* vol. 187, pp. 950–959, Jun. 2018.

[29] B. Yang et al., "Levenberg–Marquardt backpropagation algorithm for parameter identification of solid oxide fuel cells," *Int. J. Energy Res.,* vol. 45, no. 12, pp. 17903–17923, Oct. 2021.
[30] Z. W. Deng, X. S. Hu, X. K. Lin, Y. H. Che, L. Xu, and W. C. Guo, "Data-driven state of charge estimation for lithium-ion battery packs based on Gaussian process regression," *Energy,* vol. 205, Aug. 2020, Art. no. 118000.
[31] X. Hu, K. Zhang, K. Liu, X. Lin, S. Dey, and S. Onori, "Advanced fault diagnosis for lithium-ion battery systems: A review of fault mechanisms, fault features, and diagnosis procedures," *IEEE Ind. Electron. Mag.,* vol. 14, no. 3, pp. 65–91, Sep. 2020.
[32] J. C. Hong, Z. P. Wang, and Y. T. Yao, "Fault prognosis of battery system based on accurate voltage abnormity prognosis using long short-term memory neural networks," *Appl. Energy,* vol. 251, Oct. 2019, Art. no. 113381.
[33] L. Yao, Z. P. Fang, Y. Q. Xiao, J. J. Hou, and Z. J. Fu, "An intelligent fault diagnosis method for lithium battery systems based on grid search support vector machine," *Energy,* vol. 214, Jan. 2021, Art. no. 118866.
[34] S. Khaleghi, Y. Firouz, J. Van Mierlo, and P. Van den Bossche, "Developing a real-time data-driven battery health diagnosis method, using time and frequency domain condition indicators," *Appl. Energy,* vol. 255, Dec. 2019, Art. no. 113813.
[35] L. B. Jack and A. K. Nandi, "Support vector machines for detection and characterization of rolling element bearing faults," *Proc. Inst. Mech. Eng. C, J. Mech. Eng. Sci.,* vol. 215, no. 9, pp. 1065–1074, 2001.
[36] B. Xia, Y. Shang, T. Nguyen, and C. Mi, "A correlation based fault detection method for short circuits in battery packs," *J. Power Sources,* vol. 337, pp. 1–10, Jan. 2017.
[37] Z. Shiyao, C. Ziqiang, L. Jianyu, and D. Mengxue, "Cell open circuit fault diagnostic for series-parallel connected Li-ion battery pack," in *Proc. IEEE Ind. Electron. Appl. Conf.*, 2021, pp. 125–129.
[38] S. Hochreiter and J. Schmidhuber, "Long short-term memory," *Neural Comput.,* vol. 9, no. 8, pp. 1735–1780, Nov. 1997.
[39] S. Zhou, Z. Chen, D. Huang, and T. Lin, "Model prediction and rule based energy management strategy for a Plug-in hybrid electric vehicle with hybrid energy storage system," *IEEE Trans. Power Electron.,* vol. 36, no. 5, pp. 5926–5940, May 2021.

Shiyao Zhou received the M.S. degree in naval architecture and ocean engineering from the Department of Naval Architecture, Ocean and Civil Engineering, Shanghai Jiao Tong University, Shanghai, China, in 2020, where he is currently working toward the Ph.D. degree in (major) marine engineering with the State Key Laboratory of Ocean Engineering.

His current research interests are in the areas of the hybrid power system energy management and battery fault-tolerant state estimate.

Ziqiang Chen (Senior Member, IEEE) received the Ph.D. degree in mechanical engineering from Xi'an Jiaotong University, Xi'an, China, in 1999.

From 2011 to 2012, he was a visiting scholar with the Department of Electrical and Computer Engineering, Wayne State University, Detroit, MI, USA. Since 2007, he has been with Shanghai Jiao Tong University, Shanghai, China, where he is currently a Professor with the Department of Naval Architecture, Ocean and Civil Engineering. His research interests are in the areas of system identification and state estimation, fault diagnosis, discrete-event systems, automotive and electric vehicle control, battery management systems, composite energy storage system, intelligent industrial detection, robot application, and intelligent manufacturing.

Dr. Chen was the recipient of the National Scientific Conference Award, Ministerial Second Prize Award, and Excellence Award of Chinese Invention Patent.

Tiantian Lin received the B.S. degree in naval architecture and marine Engineering from Harbin Engineering University, Harbin, China, in 2017. She is currently working toward the Ph.D. degree in marine engineering with the State Key Laboratory of Ocean Engineering, Shanghai Jiao Tong University, Shanghai, China.

Her current research interests include fault diagnosis and fault-tolerant state estimate of batteries.